A Route to Complex Materials Consisting of Multiple Crystalline Phases Ir-Ru-Ir_xRu_1 − xO_2 as Multifunctional Electrocatalysts

Sarra Knani, Perla Hajjar, Marie-agnès Lacour, Arie van der Lee, Erwan Oliviero, Eddy Petit, Valerie Flaud, J Cambedouzou, Sophie Tingry, Teko Napporn, et al.

A Route to Complex Materials Consisting of Multiple Crystalline Phases Ir-Ru-$Ir_xRu_{1-x}O_2$ as Multifunctional Electrocatalysts

Sarra Knani, Perla Hajjar, Marie-Agnès Lacour, Arie van der Lee, Erwan Oliviero, Eddy Petit, Valerie Flaud, Julien Cambedouzou, Sophie Tingry, Teko W. Napporn, David Cornu, and Yaovi Holade**

S. Knani, P. Hajjar, A. van der Lee, E. Eddy, J. Cambedouzou, S. Tingry, D. Cornu, Y. Holade
Institut Européen des Membranes, IEM, UMR 5635, Univ Montpellier, ENSCM, CNRS, 34090 Montpellier, France
E-mail: david.cornu@enscm.fr (D.C.); yaovi.holade@enscm.fr (Y.H.)

M.-A. Lacour
ChemLab
ENSCM
240 Avenue du Professeur Emile Jeanbrau, 34296 Montpellier, Cedex 5 (France)

E. Oliviero, V. Flaud
Institut Charles Gerhardt, ICGM, UMR 5253, Univ Montpellier, ENSCM, CNRS, 34293 Montpellier, France

E. Oliviero
MEA Platform
Université de Montpellier
34090 Montpellier, France

J. Cambedouzou, S. Tingry, T.W. Napporn, D. Cornu, Y. Holade
French Research Network on Hydrogen (FRH2), Research Federation No. 2044 CNRS, https://frh2.cnrs.fr/
44322 Nantes Cedex 3, France

T.W. Napporn
Department of Chemistry

IC2MP CNRS UMR 7285, Université de Poitiers
4 rue Michel Brunet – B27, TSA 51106, 86073 Cedex 9 (France)

Keywords: electrocatalysis, hydrogen evolution reaction, iridium, oxides, oxygen evolution reaction, ruthenium, water electrolysis

Abstract text.

The synthesis of catalytic materials containing active sites of various oxidation states (metal, oxide, etc.) for the dual use in reduction and oxidation reactions remains challenging because most of the reported methods for the metallic state are often incompatible with those for the oxide state. We report a new methodology for the synthesis of a library of bimetallic metal-oxide materials containing three crystalline phases Ir-Ru-$Ir_xRu_{1-x}O_2$ by combining the calcination under air and the polymerization of aniline in the presence of $IrCl_3$ and $RuCl_3$ precursors. Morphology, structure, and surface oxidation state studies (XRD, SEM/EDX, S/TEM, XPS) confirm our hypothesis that $IrCl_3$ evolves to Ir while $RuCl_3$ evolves to RuO_2 during the calcination under air. An Ir:Ru atomic ratio of 50:50 can be converted into a heterogeneous nanostructure composed of Ir, Ru and $Ir_xRu_{1-x}O_2$ to date, with remarkable catalytic activity for both hydrogen evolution reaction (HER) with a small overpotential of 40 mV and oxygen evolution reaction (OER) with a small overpotential of 290 mV at the metric current density of 10 mA cm^{-2} in 0.5 M H_2SO_4. The results could serve as a platform for the development of efficient multifunctional materials for practical use in both catalytic oxidation and reduction reactions.

1. Introduction

Heterogeneous materials in which active sites of various oxidation states coexist in different phases (metals, hydroxides and oxides) are desired for the dual application in reduction and oxidation reactions.[1-4] For example, a two-phase bifunctional electrocatalyst is required to perform O_2 reduction/evolution (ORR/OER) for the reversible/regenerative fuel cell/electrolyzers or rechargeable metal-air batteries.[1,2,4] For green H_2 production by water electrolyzers,[5] metal oxides MO_2 (M = Ir, Ru) are the state-of-the-art catalysts for oxygen evolution reaction (OER, $2H_2O \rightarrow O_2 + 4H^+ + 4e^-$)[4,6-11] while metals (Rh, Pt, Ir) are suitable for hydrogen evolution reaction (HER, $2H^+ + 2e^- \rightarrow 2H_2$).[3,4,7,8,12-16] Indeed, the different oxidation states of metallic species such as metal-oxide allow to combine oxophilicity, geometric and electronic properties for better performance (activity, stability, stability).[17-20]

However, the synthesis of such materials remains challenging because the reaction atmosphere for the metallic state [reducing conditions to transform $M^{(II/III)}$ to zero valence $M^{(0)}$ (M = Ru, Ir, Pt, etc.)[3,4,7,14]] is often incompatible with that for the oxidized state [oxidizing conditions to transform $M^{(II/III)}$ to MO_x (M = Ru, Ir, etc.)[4,6,7,21]].

Because iridium-ruthenium are the state-of-the-art catalysts for the acidic water electrolyzers,[5] it is fundamental interesting to know whether M and MO_2 (M = Ir, Ru) can be synthesized and stabilized within the same material as a dual electrocatalyst for both HER and OER. For the synthesis of Ir-Ru nanostructures, reducing conditions are used in the liquid phase ($NaBH_4$, hydrothermal, etc.) or in the solid-state by calcination in the presence of H_2 (absence of O_2).[3,13,22,23] For $Ir_xRu_{1-x}O_2$, pyrolysis/calcination in the presence of air or O_2 is mainly used, and the presence of iridium metal (Ir) has been considered as a minor by-product during the decomposition of Ir(III)-Ru(III) precursors.[24,25] While calcination favors the diffusion of atoms to form an alloyed oxide $Ir_xRu_{1-x}O_2$,[24,26,27] the formation of Ir instead of IrO_2 is intriguing and not well understood. While this formation of metallic species during calcification under O_2 is counterintuitive, we have recently observed that the presence of $IrCl_3$ during the polymerization of aniline leads to the formation of Ir particles after calcination at 250-400 °C under air and $RuCl_3$ produces RuO_2 particles in the same experimental conditions.[28] The prepared polyaniline (PANI)-based materials exhibit ultrafast electrocatalytic kinetics for HER (PANI-Ir: 36 mV overpotential to reach 10 mA cm^{-2} at 21 mV dec^{-1}), OER (PANI-Ru: 240 mV overpotential to reach 10 mA cm^{-2} at 47 mV dec^{-1}) and water splitting (starting exactly at the thermo-neutral cell voltage of 1.45 V).[28]

An open question is whether a multiple-component metal-oxide catalyst Ir-Ru-$Ir_xRu_{1-x}O_2$, capable of HER and OER with intermediate activity, can be synthesized by the same calcination methodology, that is, controlling: (i) the atom diffusion to limit the formation of a single phase, (ii) the opposite kinetics of the reduction of $Ir^{(III)}$ to zero valence $Ir^{(0)}$ and the oxidation of $Ru^{(III)}$ to four valence RuO_2. Herein, we effectively synthesized for the first time, to our knowledge, a library of complex materials consisting of three crystalline phases Ir-Ru-$Ir_xRu_{1-x}O_2$ by a two steps polymerization-calcination methodology. We have investigated the elemental distribution, structure and electrocatalytic properties of the obtained heterogeneous materials through a multivariate study (SEM, EDX, XRD, S/TEM, XPS, voltammetry).

2. Results and Discussion

While the redox properties of the iridium and ruthenium species, the availability of O_2 in the furnace, and the reducing/oxidizing atmosphere created by the decomposition of polyaniline

are the key factors,[24,26,28] we hypothesized that the coexistence of metallic and oxidized states could be achieved by at least one of the scenarios shown in Figure 1a: (i) initial presence of $IrCl_3$ and $RuCl_3$ during polymerization followed by calcination (referred to as "chemical mixing" ("CM")), and (ii) separate polymerization prior to mechanical mixing of polymerized monometallic materials for calcination ("physical mixing" ("PM")). For this purpose, Ir:Ru atomic ratios of 100:0, 75:25, 50:50, 25:75, and 0:100 were studied. For electrochemical measurements, the potentials were scaled against a reversible hydrogen electrode (RHE, Figure S1).

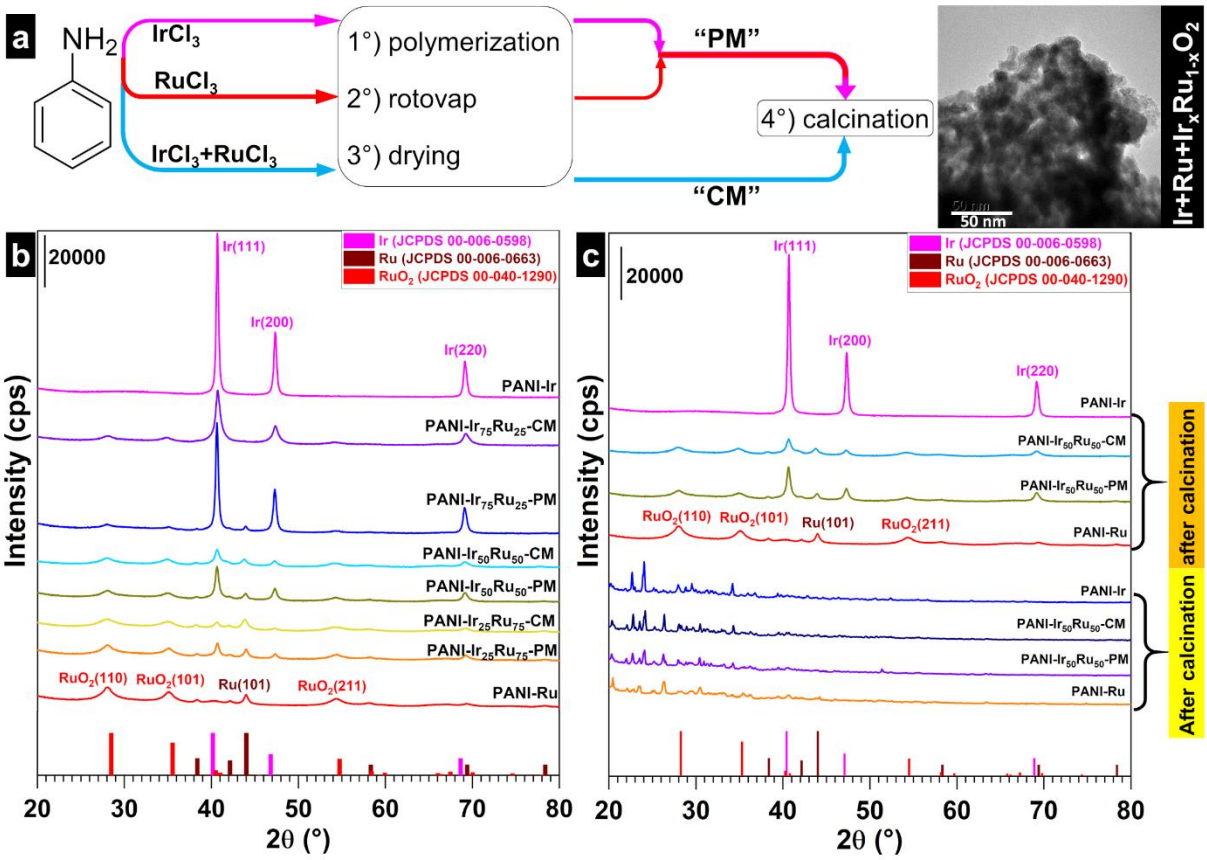

Figure 1. a) Developed methodology to access multi-phase Ir-Ru-$Ir_xRu_{1-x}O_2$ materials. b) XRD patterns. "CM": "chemical mixture" during the polymerization. "PM": "physical mixture" of the polymerized materials before the calcination. c) Effect of the calcination of the XRD patterns. "CM" referred to as "chemical mixture" during the polymerization and "PM" means "physical mixture" by mechanical mixing the polymerized monometallic-based materials before the calcination.

The oxidative polymerization of aniline to polyaniline (PANI) was performed in hydrochloric acid as the doping acid and in the presence of ammonium persulfate as the

oxidizing agent, producing mainly the emeraldine form of PANI.[29,30] The calcination program under air consisted of heating at 2° C min^{-1} up to 250, 350, and 400 °C (1 h dwell each, Figure S2 and Scheme S1). While such calcination under air is expected to lead to the formation of oxides,[24,26] preliminary thermogravimetric and differential thermogravimetric analysis (TGA-DTA, Figure S2) showed a lower metal content for PANI-Ir compared to PANI-Ru, which may indicate a different nature of the products.

X-ray diffraction (XRD) was used to determine the structure and composition of the materials. Figures 1b-c and S3 (and Tables 1, S1-S2) show the obtained results. Monometallic PANI-Ir consists of 100% of cubic phase of Ir (lattice parameters: $a = b$ = c = 3.840 Å; d-spacing: 2.217 Å for Ir(111)). PANI-Ru consists of 90 wt% of quadratic RuO_2 phase (lattice parameters: $a = b$ = 4.494 Å and c = 3.108 Å; d-spacing: 3.176 Å for RuO_2(110)) and 10 wt% of hexagonal Ru (lattice parameters: $a = b$ = 2.710 Å and c = 4.284 Å; d-spacing: 2.058 Å for Ru(101)). Bimetallic materials have the diffraction peaks of $Ir_xRu_{1-x}O_2$, Ru and Ir, validating our hypothesis of successful synthesis of separate phases rather than a single $Ru_xIr_{1-x}O_2$ by at least one of the two strategies of Figure 1a. Figure 1c clearly highlights that the majority of Ir and RuO_2 are formed after the calcination, starting with monometallic precursors. Indeed, the diffraction peaks are mainly below 40° for the non-heat treated materials, assigned to PANI and metals salts.[29,31,32] Furthermore, although IrO_2 and RuO_2 have the same structure (rutile) and the cation radius of Ir^{4+} and Ru^{4+} is similar (~0.62 Å),[24-26,33] we ruled out IrO_2 and RuO_2 phase segregation because IrO_2 does not form in the absence of ruthenium. The formation of metallic species in addition to oxides was reported,[24,25] however, the 61-65, 33-36, and 22-24 wt% Ir+Ru achieved with Ir:Ru atomic ratios of 75:25, 50:50, and 25:75, respectively, are the highest values to date. Based on these results, we can hypothesize that bimetallic materials will be active for both HER (benefiting from the metallic character) and OER (benefiting from the oxide character).

Table 1. Phases composition from XRD.

Entry[a)]	Ir	$Ir_{75}Ru_{25}$-CM	$Ir_{75}Ru_{25}$-PM	$Ir_{50}Ru_{50}$-CM	$Ir_{50}Ru_{50}$-PM	$Ir_{25}Ru_{75}$-CM	$Ir_{25}Ru_{75}$-PM	Ru
$Ir_xRu_{1-x}O_2$ (wt%)	0	35.1 ± 0.7	39.0 ± 1.1	64.3 ± 0.8	67.0 ± 1.6	76.5 ± 0.5	77.8 ± 0.6	89.7 ± 1.1
Ru (wt%)	0	0	2.6 ± 0.2	15.5 ± 0.3	6.8 ± 0.2	18.0 ± 0.2	11.9 ± 0.2	10.3 ± 0.3
Ir (wt%)	100	64.9 ± 0.6	58.4 ± 0.7	20.2 ± 0.3	26.2 ± 0.4	5.5 ± 0.1	10.3 ± 0.1	0

[a)] "CM": "chemical mixture" during the polymerization. "PM": "physical mixture" of the polymerized materials before the calcination.

To further characterize the morphology and precisely localize the elemental distribution at both the micro and atomic scales, we next performed a series of electron microscopy analysis. The atomic scale elemental maps of the different elements by scanning transmission electron microscopy coupled energy-dispersive X-ray spectroscopy (STEM-EDX) from Figure 2a-d are in agreement with bulk analysis by scanning electron microscopy coupled energy-dispersive X-ray spectroscopy (SEM-EDX) after calcination (Figures S4-S19). Control SEM-EDX analysis prior to calcination (Figures S20-S27) only show the initial precursors, which are $IrCl_3$ and $RuCl_3$ (at least the Ir, Ru and Cl signals overlap). The typical (HR)TEM images of the materials after the calcination are reported in Figures S28-S31. For monometallic materials, the Ir and O signals do not overlap for PANI-Ir (Figure 3a, Figure S4), while those of Ru and O overlap in PANI-Ru where the atomic ratio O/Ru is ~2.0 (Table S3, Figure 3b, Figure S6), which is agreement with the STEM-EDX line profiles (Figure S32a-b). The presence of oxygen species in PAN-Ir after calcination results from the natural oxidation of a metal when exposed to air, since quantitative XRD analysis revealed no significant quantity of IrO2 and, as we will later see, electrochemistry confirmed the metallic character. For PANI-Ir the *d*-spacing values in Figure S33 of 2.3 and 2.0 Å correspond to, respectively, (111) and (200) of Ir. For PANI-Ru, the *d*-spacing value of 3.2 Å (Figure S34) corresponds to (110) of RuO_2. These outcomes confirm the previous XRD results that PANI-Ir leads to Ir while PANI-Ru leads to RuO_2.

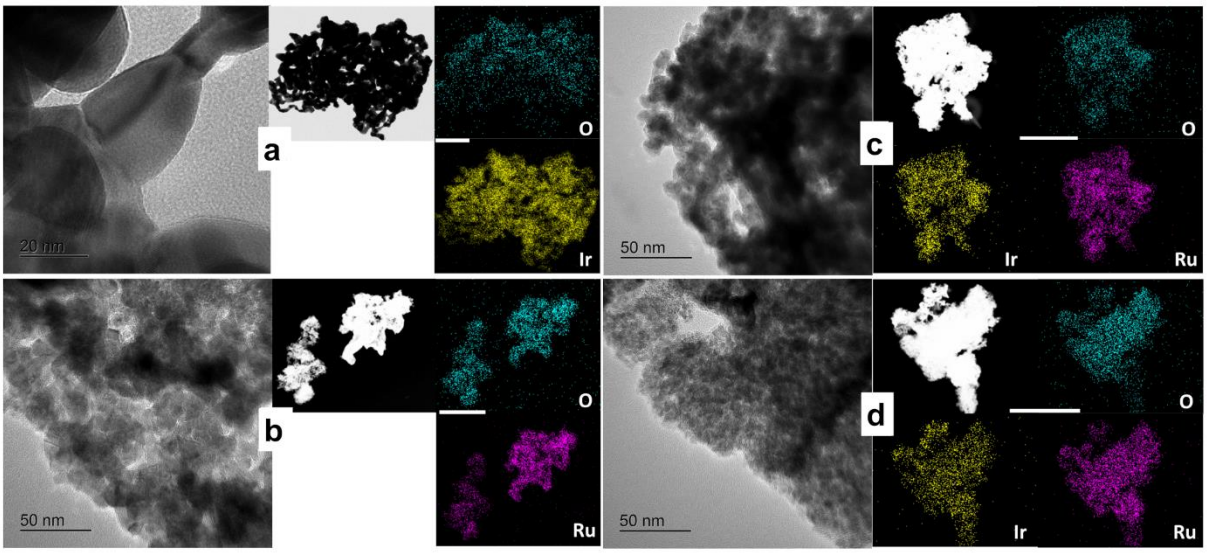

Figure 2. Bright-field TEM and dark-field STEM images. In colors, STEM-EDX elemental maps (scale bar = 250 nm) for materials derived from: a) PANI-Ir, b) PANI-Ru, c) PANI-$Ir_{50}Ru_{50}$-PM, and d) PANI-$Ir_{50}Ru_{50}$-CM.

For bimetallic materials, Figures 2c-d and S32 suggest that some Ru, Ir and O coexist at the atomic scale, which is supported by the STEM-EDX line profiles (Figure S32c-d) and *d*-spacing values of Figures S35-S36 (3.0-3.3 Å corresponds to (110) of $Ru_xIr_{1-x}O_2$ and 2.2-2.3 Å corresponds to (111) of Ir). Conclusively, these electron microscopy analyses are consistent with XRD results and support the formation of heterogeneous materials composed of Ir, Ru and $Ir_xRu_{1-x}O_2$. The specific surface area (BET) from the N_2 adsorption-desorption isotherms for representative materials (Figure S37) shows that the current materials have a high surface area, 103 $m^2\ g^{-1}$ for PANI-Ru (RuO_2 structure) and 60-84 $m^2\ g^{-1}$ for bimetallic, whereas the commonly reported values are in the range of 20-40 $m^2\ g^{-1}$.[24,26,33]

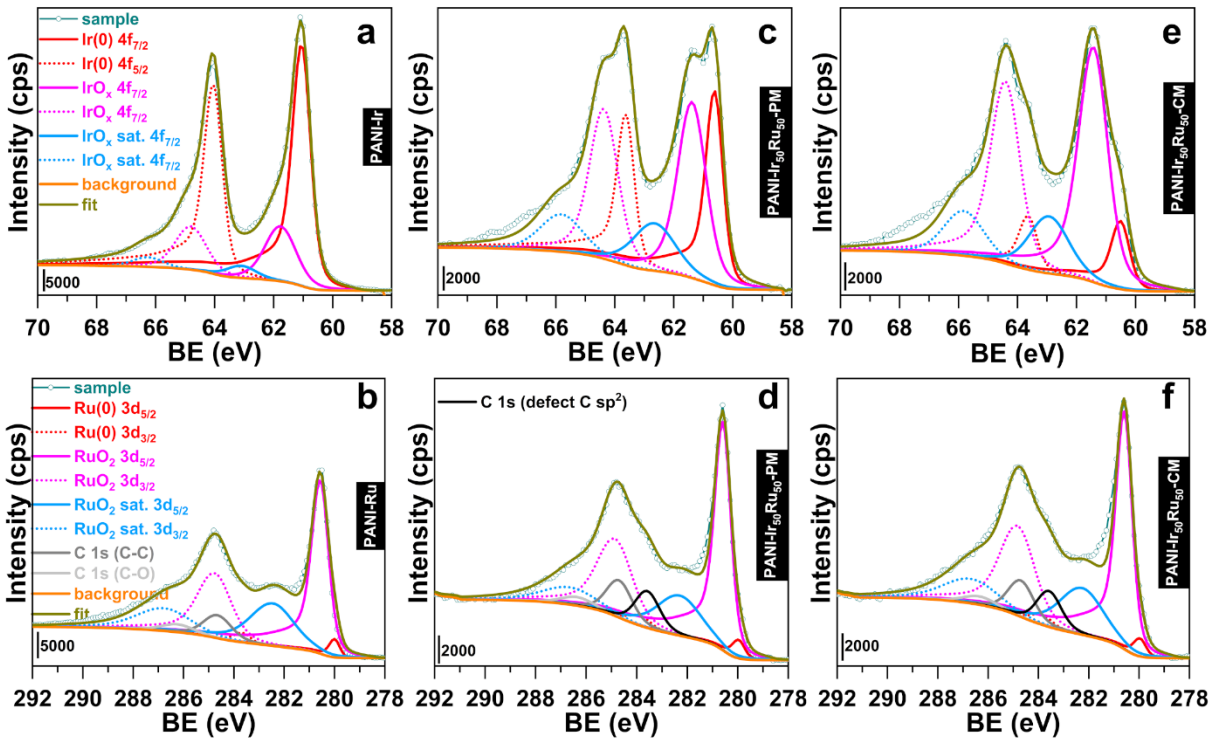

Figure 3. High-resolution XPS spectra of Ir 4f and Ru 3d for: a) PANI-Ir, b) PANI-Ru, c-d) PANI-$Ir_{50}Ru_{50}$-PM, and e-f) PANI-$Ir_{50}Ru_{50}$-CM.

We next determined the oxidation state of the different elements by X-ray photoelectron spectroscopy (XPS). We used the NIST standard reference database 20 version 4.1 (Table S4) for the assignment and the Ru 3d core-level to fit ruthenium.[25,34] Survey XPS spectra (Figure

S38) confirm the elements identified by EDX. High resolution XPS (Figures 3a-f, S39 and Table S5) confirms that PANI-Ru leads to RuO_2, while PANI-Ir produces Ir (the oxidized species are simply due to natural oxidation upon exposure to ambient air, as no oxide peak was detected in the XRD patterns). The increased intensity of the metallic component of Ir 4f in Figure 3c compared to Figure 3e (in agreement with Table 1 for Ru:Ir = 50:50) can be explained by the limited diffusion of atoms that are randomly distributed when the material results from mechanical mixing, referred to as "PM".

The previous results show the ability to synthesize complex materials consisting of three crystalline phases Ir-Ru-$Ir_xRu_{1-x}O_2$. The formation of such materials could be explained by several factors, such as the discrepancy in the redox properties of the cationic species of iridium and ruthenium, the availability of oxygen in the calcination furnace, and the presence of polyaniline in the starting material, the combustion of which could provide a mixture of oxidative and reductive environments. Further study is needed for the origin of the selective heat treatment in air, for example by coupling TGA-DSC to MS and testing different iridium and ruthenium precursors, possibly at different valences. XRD results showed a shift in the position of the main Ir(111) peak to higher 2θ values in the bimetallic materials compared with monometallic PANI-Ir as the amount of ruthenium increased. For the main oxide peak, i.e. $Ir_xRu_{1-x}O_2$(110), the shift was not significant, but the intense main peak of the hexagonal Ru phase shifts, which could be attributed to the difference in crystallographic parameters of the structures. As a result, the structural parameters of the metal and oxide species are markedly different as a function of phase fraction, suggesting a possible positive impact on catalytic activity due to the presence of electronic and synergistic interactions as well as the heterogeneous interface between the different phases.

Finally, the electrochemical properties were accessed (Figures 4, 5 and S40). We first used cyclic voltammetry (CV) in a 0.5 M H_2SO_4 electrolyte to check whether the synthesized materials behave like metals or oxides. On the one hand, Figure S40a shows that the voltammogram of PANI-Ru is characteristic of RuO_2: (i) absence of a hydrogen region at 0-0.4 V_{RHE}, and (ii) the presence of redox footprints above 0.6 V_{RHE} for the $Ru^{(IV)}/Ru^{(V)}$ involved in OER.[24-26,33,34] On the other hand, Figure 40b demonstrates that PANI-Ir has the behavior of a Pt-like metal with a reversible proton adsorption/desorption processes in the 0.05-0.40 V_{RHE} region.[12,22,35] Taken together, these results means that PANI-Ir material should be active for HER, while PANI-Ru would be suitable for OER. Furthermore, consistent with the previous physico-chemical characterization, the bimetallic materials exhibit mixed voltammetry profiles of both oxides and metals. This behavior was further confirmed by the double layer capacitance

(C_{dl}) measurements (Figure S41) for accessing the electrochemically active surface area (ECSA = C_{dl}/C_s, C_s = reference capacitance of the monolayer, which value depends on the nature of the electrode material,[36-38] ranging from 11 to 130 µF cm^{-2}). Specifically, C_{dl} = 4.4, 1.1, and 1.6-4.1 mF cm^{-2} for PANI-Ru, PANI-Ir, and PANI-Ru-Ir, respectively.

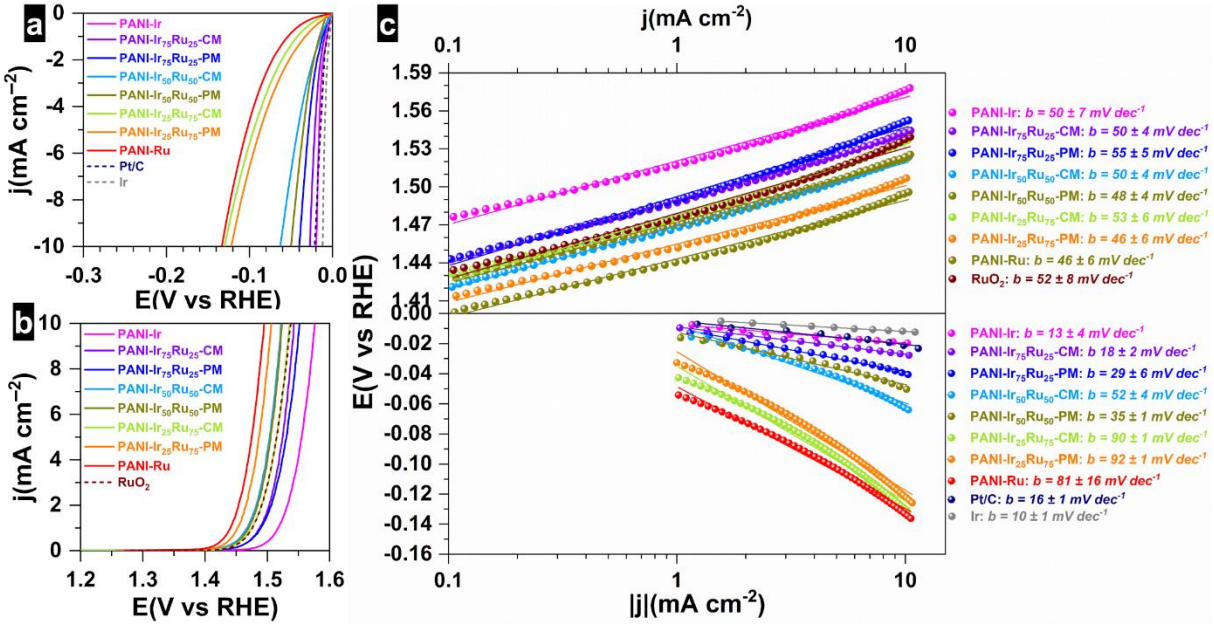

Figure 4. a-b) Linear Sweep Voltammetry (LSV, 0.005 V s^{-1}, 0.5 M H_2SO_4, 25 °C) polarization curves: a) HER, and b) OER. c) The corresponding Tafel plots from LSV (obtained at 0.005 V s^{-1} in 0.5 M H_2SO_4 electrolyte at 25 °C): OER (top) and HER (bottom).

To verify that the bimetallic materials are active for both HER and OER, while being intermediate between RuO_2 (OER) and Ir (HER), we next performed linear sweep voltammetry (LSV, Figure 4), chronopotentiometry (Figure S42), and electrochemical impedance spectroscopy (EIS, Figures 5, S43 and Table S6). Overall, the performance is analogous to that of reference materials (Pt/C and Ir for HER, and RuO_2 for OER) and the literature (Tables S7-S8). Specifically, LSV of HER (Figure 4a) shows that the overpotential needed to reach the metric current density of |j| = 10 mA cm^{-2} is 20 and 134 mV for PANI-Ir and PANI-Ru, which confirms the Pt-like characteristic of the synthesized PANI-Ir while PANI-Ru that is mainly composed of RuO_2 is not much active for HER. For OER, PANI-Ru is more efficient than PANI-Ir, with overpotentials of 0.27, and 0.35 V at 10 mA cm^{-2}, respectively. These data are substantiated by the stability tests performed by chropotentiometry at the current density of |j| = 10 mA cm^{-2} (Figure 4c) and EIS at different electrode potentials (Figure 5a-c). To evaluate the Tafel slope, we have implemented two independent methods, the LSV (Figure 4c) and the

EIS at different applied potentials (Figure 5c). The fitted EIS data by R_Ω+Q_{CPE}//R_{ct} are gathered in Table S6; R_Ω, Q_{CPE} and R_{ct} represent the uncompensated ohmic resistance, the constant phase element, and the charge transfer resistance, respectively.[39,40] The method of the charge transfer resistance (R_{ct}) determined by EIS enables to probe only the electron transfer ability at different electrode potentials,[34,41,42] which allows to eliminate the possible contribution of non-faradaic processes to LSV curves. We note that the experimental values of the Tafel slope can deviate from the theoretical metrics for several reasons, the thickness/compactness of the catalytic layer, the contribution of mass transport, the faradic processes associated with electrocatalyst itself, etc.[34,43-48] Mechanistically, the main three steps of HER and the corresponding Tafel slopes at 25 °C are described by Eqs. (1-3), the overall reaction is Eq. (4) (Tafel slopes corresponds to 25 °C). For HER, when Ir is the main constituent, the reaction seems to be under H_2 evolution limitation by Heyrovsky step ($H_{(ads)} + H^+_{(aq)} + e^- \rightarrow H_2$) and Tafel step ($H_{(ads)} + H_{(ads)} \rightarrow H_2$). When Ru predominates, the Tafel slope is higher than 40 mV dec^{-1}, suggesting that the HER kinetics might be under both hydrogen adsorption limitation (Volmer step, $H^+_{(aq)} + e^- \rightarrow H_{(ads)}$) and H_2 evolution step of Heyrovsky step ($H_{(ads)} + H^+_{(aq)} + e^- \rightarrow H_2$).

$$H^+_{(aq)} + e^- \rightarrow H_{(ads)} \qquad b = 118 \text{ mV dec}^{-1} \qquad (1)$$

$$H_{(ads)} + H^+_{(aq)} + e^- \rightarrow H_2 \qquad b = 39 \text{ mV dec}^{-1} \qquad (2)$$

$$H_{(ads)} + H_{(ads)} \rightarrow H_2 \qquad b = 29 \text{ mV dec}^{-1} \qquad (3)$$

$$\text{Overall: } 2H^+ + 2e^- \rightarrow H_2 \qquad (4)$$

The elementary steps of OER are described by Eqs. (5-8), the overall reaction is Eq. (9) (Tafel slopes corresponds to 25 °C).

$$H_2O \rightarrow OH_{ads} + H^+ + e^- \qquad b = 118 \text{ mV dec}^{-1} \qquad (5)$$

$$OH_{ads} \rightarrow O_{ads} + H^+ + e^- \qquad b = 39 \text{ mV dec}^{-1} \qquad (6)$$

$$OH_{ads} + OH_{ads} \rightarrow O_{ads} + H_2O \qquad b = 29 \text{ mV dec}^{-1} \qquad (7)$$

$$2O_{ads} \rightarrow O_2 \qquad b = 29 \text{ mV dec}^{-1} \qquad (8)$$

$$\text{Overall: } 2H_2O \rightarrow O_2 + 4H^+ + 4e^- \qquad (9)$$

For OER, both methods lead to Tafel slopes of 45-60 mV dec^{-1}, which indicate that the deprotonation of the adsorbed hydroxyl species (from the first step of water splitting) is the limiting step.[34,49,50] Taking advantage of the structural characteristics (morphology, structure and coexistence of 20-26 wt% Ir, 7-15 wt% Ru and 64-67 wt% $Ir_xRu_{1-x}O_2$), PANI-$Ir_{50}Ru_{50}$ has a reduced charge-transfer resistance, leading to a low overpotential for both HER (40 mV) and OER (290 mV) at the metric current density of 10 mA cm^{-2}. The main reason for such behavior

could be the heterogeneous composition exhibiting a metal-like behavior for ca. 35 ± 5 wt% of Ir+Ru that is appropriate for HER and an oxide-like behavior for ca. 65 ± 5 wt% of $Ir_xRu_{1-x}O_2$ that is suitable for OER, as sketched in Figure 5d. The previously found $Ir_xRu_{1-x}O_2$(110) by the electron microscopy could explain the high activity for OER because seminal density functional theory (DFT) calculations by Rossmeisl et al.[51] suggested that the optimal binding energy of the oxygenated and hydroxyl intermediates of OER is reached at MO_2 (M = Ru, Ir) surface. The heterojunction between the different phases could contribute to the catalytic activity. We point out that the catalytic ink needs to be strengthened before considering the real application, as the ink stability was not satisfactory (Figure S42). Nevertheless, our results can inspire the development of multifunctional catalysts for use in both oxidation and reduction reactions.

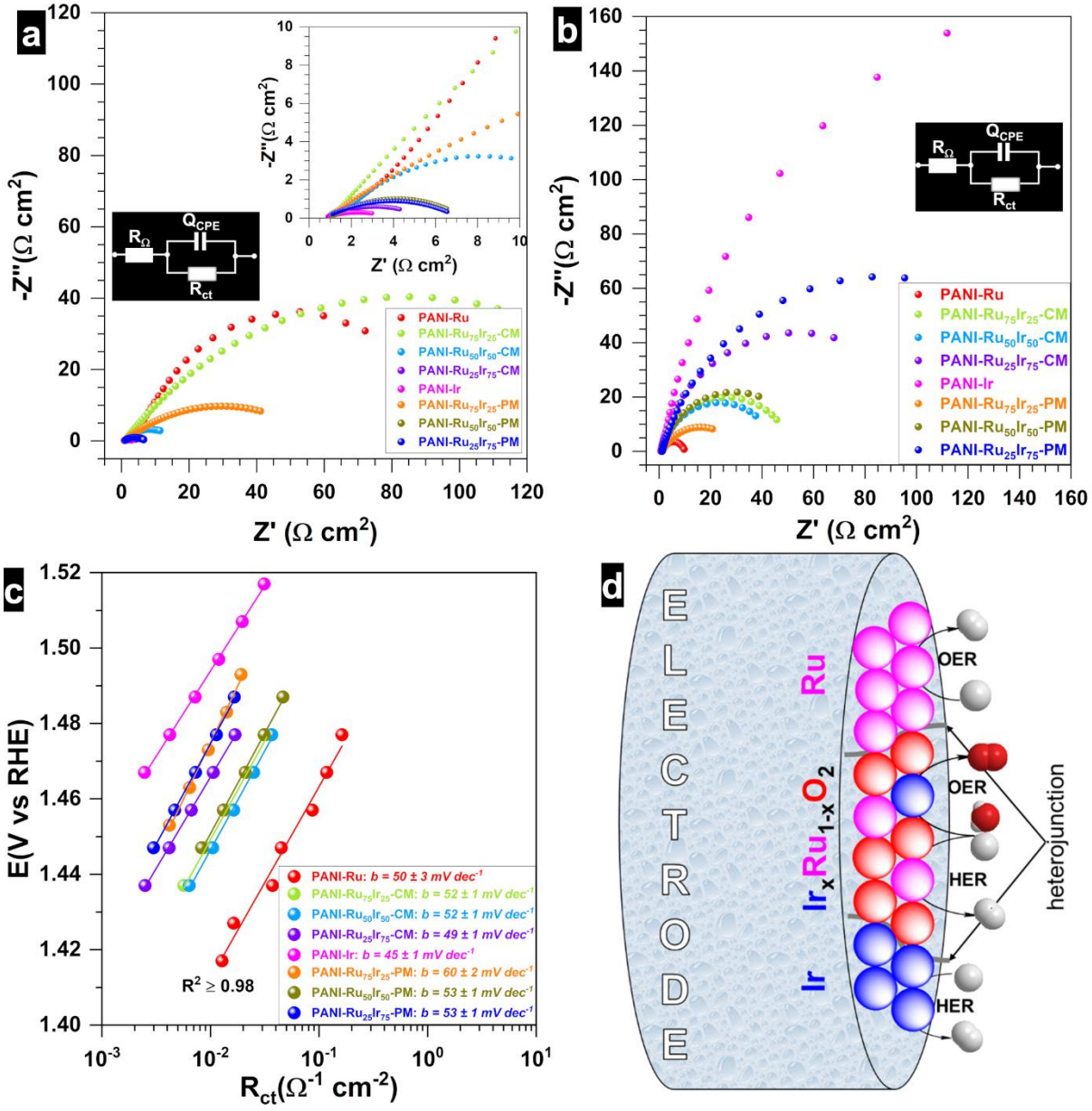

Figure 5. a) Complex-plane Nyquist impedance (normalized by the electrode area) at E_{appl} = -0.02 V vs RHE (iR-drop uncorrected) for HER in 0.5 M H_2SO_4 at 25 °C: inset the equivalent electrical circuit R_Ω + Q_{CPE}//R_{ct}. b) Complex-plane Nyquist impedance (normalized by the electrode area) at E_{appl} = 1.47 V vs RHE (iR-drop uncorrected) for OER in 0.5 M H_2SO_4 at 25 °C: inset the equivalent electrical circuit R_Ω + Q_{CPE}//R_{ct}. c) R_{ct}-based Tafel plots for OER in 0.5 M H_2SO_4 at 25 °C. d) Sketch of the operation of a multifunctional HER-OER electrocatalyst.

3. Conclusion

In summary, we have demonstrated a new methodology that combines polymerization and calcination to synthesize a library of metal-oxide materials containing three phases, Ir, Ru and $Ir_xRu_{1-x}O_2$, referred to as Ir-Ru-$Ir_xRu_{1-x}O_2$. The nature of MCl_3 (M = Ir, Ru) precursor during the polymerization results in a difference in composition after the calcination as well as a tunable catalytic performance. Mechanical mixing prior to calcination limits atom diffusion resulting in a heterogeneous, Ir-Ru-$Ir_xRu_{1-x}O_2$, which is active for both HER and OER. This report will serve as a platform for the development of efficient synthesis methods for multifunctional catalysts. Ongoing research focuses on optimizing catalytic ink formation to improve stability in a membrane-electrode-assembly (MEA), as well as characterizing the origin of the selective heat treatment under air.

4. Experimental Methods

Chemicals and Materials: Aniline (ANI, 100%, Alfa Aesar, Haverhill, MA, USA), Ruthenium (III) chloride hydrate ($RuCl_3 \cdot xH_2O$, Premion®, 99.99%, Alfa Aesar, Germany), iridium (III) chloride hydrate ($IrCl_3 \cdot xH_2O$, 99.8%, Alfa Aesar, Germany), hydrochloric acid (HCl, 37%, VWR, France), ammonium persulfate ($(NH_4)_2S_2O_8$, APS, 98%, Alfa Aesar, Germany), isopropanol (iPrOH, 99.5%, Sigma Aldrich, St. Louis, MO, USA), Nafion® suspension (5 wt%, Sigma Aldrich, St. Louis, MO, USA), sulfuric acid (H_2SO_4, 95-97 % Supelco, Switzerland), RuO_2 (Permeteck, USA, Ir (Permeteck, USA) and Pt/C (Permeteck, USA) were used as received. Water was produced from a Milli-Q Millipore source (18.2 MΩ cm at 20 °C).

Synthesis: Ruthenium and iridium materials modified polyaniline (PANI) with different atomic ratio of Ru:Ir were synthesized according the method illustrated in Scheme S1 and inspired by our previous oxidative aniline polymerization and calcination.[28,52] Briefly, an aqueous solution containing 0.4 M aniline, 0.5 M HCl and appropriate metal precursor(s) was prepared (50 mL, 10.7 $mg_{(total\ metal)}$ per mL) and placed in a double-jacket reactor at 5 °C. A

second solution containing 0.5 M HCl and 0.2 M APS was prepared (50 mL). The, under vigorous stirring, the second solution was then added to the first one at 5 mL per minute through a two-syringe infusion pump (KD Scientific). The mixture begins to change color until a stable color is obtained (the nature of which depends on the type of metal precursor), indicating the polymerization of aniline.[29] The reaction was continued for 15 h. The solvent was removed from the mixture by rotavap and the solid phase was dried in an oven at 80 °C for 12 h. For the final thermal treatment under air (ashes furnace, Vecstar), the temperature program was a heating at 2 °C min^{-1} up to 250, 350, and 400 °C (1 h dwell each, see Scheme S1) by adopting two strategies to synthesize a library of eight (8) samples:

- Two monometallic-based materials referred to as a PANI-Ru and PANI-Ir, which means that the polymerization was performed in presence of single monometallic precursor,
- Three bimetallic-based materials referred to as a PANI-$Ru_{75}Ir_{25}$-CM, PANI-$Ru_{50}Ir_{50}$-CM and PANI-$Ru_{25}Ir_{75}$-CM; "CM" stands for "chemical mixture", which means that the polymerization was performed in presence of both monometallic precursors,
- Three bimetallic-based materials referred to as a PANI-$Ru_{75}Ir_{25}$-PM, PANI-$Ru_{50}Ir_{50}$-PM and PANI-$Ru_{25}Ir_{75}$-PM; "PM" stands for "physical mixture", which means that the polymerization was performed separately for each monometallic precursor followed by grinding in mortar the appropriate mixture of Ru:Ir molar ratio.

Physicochemical Characterization: Thermogravimetric analysis (TGA) and differential thermogravimetric analysis (DTA) were performed with SDT Q600 TA Instruments using aluminum crucibles in the temperature range of room temperature to 400 °C at 2 °C min^{-1} under air flow of 100 mL min^{-1} (Scheme S1 for further details). X-ray diffraction (XRD) was performed on a PANalytical Xpert-PRO diffractometer (Malvern Panalytical, Almelo, the Netherlands) (40 kV, 20 mA) equipped with a copper anode at $\lambda(CuK_\alpha)$ = 1.54 Å, and in Bragg-Brentano mode (with 2θ = 20–80°). A quantitative phase analysis was performed using the Fullprof program,[53] interfaced by WinPlotR. The atomic structures of Ru (54236-ICSD), Ir (640730-ICSD), and RuO_2 (172178-ICSD) were retrieved from the Inorganic Crystal Structure Database[54] and kept fixed during the subsequent calculations. Pseudo-Voigt profile functions were used to model the peak shapes. During the first cycles of the refinements, the scale factors and profile parameters were optimized and also an overall zero-shift parameter, after which the cell parameters were refined as well. The refined cell parameters are less reliable for the minority phases. The structural parameters are calculated on the basis of Rietveld method. Scanning electron microscopy (SEM) and energy-dispersive X-ray spectroscopy (EDX) analyses were carried out on Hitachi S-4800 FEG, and ZEISS EVOHD 15 microscopes,

respectively. Scanning transmission electron microscopy (STEM), High-angle annular dark-field (HAADF)–STEM and EDX mapping with line scanning analysis were was performed on FEG JEOL 2200FS microscope operated at 200 kV accelerating voltage. N_2 adsorption-desorption measurements were conducted on Micromeritics ASAP 2020 instruments. X-ray photoelectron spectroscopy (XPS) characterization was performed on a Thermo Electron ESCALAB 250 spectrometer equipped with a monochromatic radiation source Al Mono ($Al_{k\square}$ = 1486.6 eV) operating at 15 kV and 6 mA (survey at a step of 1 eV for transition energy of 150 eV and high-resolution at 0.1 eV for transition energy of 20 eV). The binding energies were corrected on the basis of the energy of C1s at 284.4 eV by using the AVANTAGE software for peaks fitting. The quantification was carried out from the peak area after correction with a suitable sensitivity factor.

Electrochemical Measurements: All the electrochemical tests were carried out at controlled temperature of 25 °C in a conventional three-electrode cell (single compartement) using the potentiostat Autolab PGSTAT 128N (Metrohm, Netherland). The electrochemical system consists of: (i) the working electrode was a glassy carbon part of rotating disk electrode (RDE, Metrohm Autolab, 0.196 cm^2), (ii) the counter electrode was a glassy carbon slab (12 cm^2), and (iii) the reference electrode was Ag|AgCl|(KCl, 3M), referred to as "Ag/AgCl". In this work, all the electrode potentials were referenced to reversible hydrogen electrode (RHE) using the calibration method illustrated by Figure S1, and described by Eq. (10).

$$E(\text{V vs RHE}) = E(\text{V vs Ag/AgCl}) + \Delta E,\ \Delta E = 0.217\ \text{V} \quad (10)$$

The catalytic ink composition consisted of 260 µL water, 100 µL isopropanol, 50 µL Nafion® suspension (5 wt% in alcohols, Sigma Aldrich) and 4 mg catalyst. First, only the liquid phase is sonicated in a water bath for 15 min. The catalytic powder is then added and the suspension is sonicated for 30 min to obtain a homogeneous catalytic ink. Before dropping the catalyst onto the glassy carbon electrode, the latter was polished with alumina powder of different diameters (1, 0.3 and 0.05 µm) until a mirror-like surface was obtained. The glassy carbon electrode was then sonicated and washed three times, alternating between water and ethanol. Finally, a volume of 4 µL of the catalyst ink was dropped on the glassy carbon electrode

and dried at 100 rpm for 5 min and 400 rpm for 10 min to evaporate the solvent and obtain a homogeneous thin-film. The metal loading was estimated to be 0.2 mg cm^{-2} for all the materials prepared and 0.1 mg cm^{-2} for the benchmark Pt/C. The electrolyte was 0.5 M H_2SO_4. Cyclic voltammetry (CV) experiments were carried out over a potential range from 0.05 to 1.20 V vs. RHE in an Ar-saturated electrolyte solution, at different scan rates (from 200 to 10 mV s^{-1}). Linear sweep voltammetry (LSV) was performed at 1600 rpm in H_2-satured electrolyte for HER and in O_2-saturated electrolyte for OER, at 5 mV s^{-1}. Electrochemical impedance spectroscopy (EIS) was carried out over a frequency range from 100 kHz to 1 Hz at different electrode potentials (see main text). Chronopotentiometry (CP) was performed at $|j| = 10$ mA cm^{-2} for 0.5 h. LSV curves of HER and OER were iR-drop corrected by ohmic resistance determined from EIS.

Supporting Information

Supporting Information is available from the Wiley Online Library or from the author.

Acknowledgements

This work was supported by LabEx CheMISyst (ANR-10-LABX-05-01) and by CNRS Energy Unit (PEPS21-CALEX4H2). We thank Nathalie Masquelez, Bertrand Rebiere and Didier Cot for assistance with SEM-EDX/TGA-DTA analysis.

Received: ((will be filled in by the editorial staff))
Revised: ((will be filled in by the editorial staff))
Published online: ((will be filled in by the editorial staff))

References

[1] M. Klingenhof, P. Hauke, S. Brückner, S. Dresp, E. Wolf, H. N. Nong, C. Spöri, T. Merzdorf, D. Bernsmeier, D. Teschner, R. Schlögl, P. Strasser, *ACS Energy Lett.* **2021**, *6*, 177.

[2] S. Dresp, F. Luo, R. Schmack, S. Kuhl, M. Gliech, P. Strasser, *Energy Environ. Sci.* **2016**, *9*, 2020.

[3] H. Wang, H. D. Abruña, *ACS Catal.* **2019**, *9*, 5057.

[4] B. Paul, J. Andrews, *Renew. Sustain. Energy Rev.* **2017**, *79*, 585.

[5] M. Chatenet, B. G. Pollet, D. R. Dekel, F. Dionigi, J. Deseure, P. Millet, R. D. Braatz, M. Z. Bazant, M. Eikerling, I. Staffell, *Chem. Soc. Rev.* **2022**, *51*, 4583.

[6] L. Wang, V. A. Saveleva, S. Zafeiratos, E. R. Savinova, P. Lettenmeier, P. Gazdzicki, A. S. Gago, K. A. Friedrich, *Nano Energy* **2017**, *34*, 385.
[7] Y.-B. Cho, A. Yu, C. Lee, M. H. Kim, Y. Lee, *ACS Appl. Mater. Interfaces.* **2018**, *10*, 541.
[8] H. Schäfer, M. Chatenet, *ACS Energy Lett.* **2018**, *3*, 574.
[9] N. Danilovic, R. Subbaraman, K. C. Chang, S. H. Chang, Y. Kang, J. Snyder, A. P. Paulikas, D. Strmcnik, Y. T. Kim, D. Myers, V. R. Stamenkovic, N. M. Markovic, *Angew. Chem. Int. Ed.* **2014**, *53*, 14016.
[10] L. Gloag, T. M. Benedetti, S. Cheong, Y. Li, X.-H. Chan, L.-M. Lacroix, S. L. Y. Chang, R. Arenal, I. Florea, H. Barron, A. S. Barnard, A. M. Henning, C. Zhao, W. Schuhmann, J. J. Gooding, R. D. Tilley, *Angew. Chem. Int. Ed.* **2018**, *57*, 10241.
[11] S. Kim, O. Kwon, C. Kim, O. Gwon, H. Y. Jeong, K.-H. Kim, J. Shin, G. Kim, *Advanced Materials Interfaces* **2018**, *5*, 1800123.
[12] J. Zheng, W. Sheng, Z. Zhuang, B. Xu, Y. Yan, *Sci. Adv.* **2016**, *2*, Article number: e1501602.
[13] D. Wu, K. Kusada, S. Yoshioka, T. Yamamoto, T. Toriyama, S. Matsumura, Y. Chen, O. Seo, J. Kim, C. Song, S. Hiroi, O. Sakata, T. Ina, S. Kawaguchi, Y. Kubota, H. Kobayashi, H. Kitagawa, *Nat. Commun.* **2021**, *12*, 1145.
[14] Y. Zheng, Y. Jiao, Y. Zhu, L. H. Li, Y. Han, Y. Chen, M. Jaroniec, S.-Z. Qiao, *J. Am. Chem. Soc.* **2016**, *138*, 16174.
[15] Y. Yao, S. Hu, W. Chen, Z.-Q. Huang, W. Wei, T. Yao, R. Liu, K. Zang, X. Wang, G. Wu, W. Yuan, T. Yuan, B. Zhu, W. Liu, Z. Li, D. He, Z. Xue, Y. Wang, X. Zheng, J. Dong, C.-R. Chang, Y. Chen, X. Hong, J. Luo, S. Wei, W.-X. Li, P. Strasser, Y. Wu, Y. Li, *Nat. Catal.* **2019**, *2*, 304.
[16] F. Wang, S. Qin, B. Zhu, P. Jin, J. Cai, Y. He, H. Cong, L. Feng, *Advanced Materials Interfaces* **2022**, *9*, 2101564.
[17] T. Zhao, Y. Hu, M. Gong, R. Lin, S. Deng, Y. Lu, X. Liu, Y. Chen, T. Shen, Y. Hu, L. Han, H. Xin, S. Chen, D. Wang, *Nano Energy* **2020**, *74*, Article number: 104877.
[18] D. Strmcnik, M. Uchimura, C. Wang, R. Subbaraman, N. Danilovic, V. van der, A. P. Paulikas, V. R. Stamenkovic, N. M. Markovic, *Nat. Chem.* **2013**, *5*, 300.
[19] A. M. R. Ramírez, S. Heidari, A. Vergara, M. V. Aguilera, P. Preuss, M. B. Camarada, A. Fischer, *ACS Mater. Au* **2023**, *3*, 177.
[20] J. Resasco, F. Abild-Pedersen, C. Hahn, Z. Bao, M. T. M. Koper, T. F. Jaramillo, *Nat. Catal.* **2022**, *5*, 374.
[21] J. Ruiz Esquius, D. J. Morgan, G. Algara Siller, D. Gianolio, M. Aramini, L. Lahn, O. Kasian, S. A. Kondrat, R. Schlögl, G. J. Hutchings, R. Arrigo, S. J. Freakley, *J. Am. Chem. Soc.* **2023**, *145*, 6398.
[22] H.-S. Oh, H. N. Nong, T. Reier, M. Gliech, P. Strasser, *Chem. Sci.* **2015**, *6*, 3321.
[23] S. Wang, S. Yang, Z. Wei, Y. Liang, J. Zhu, Y. Tang, X. Qiu, *J. Mater. Chem. A* **2022**, *10*, 25556.
[24] N. Mamaca, E. Mayousse, S. Arrii-Clacens, T. W. Napporn, K. Servat, N. Guillet, K. B. Kokoh, *Appl. Catal. B: Env.* **2012**, *111-112*, 376.
[25] D. Escalera-López, S. Czioska, J. Geppert, A. Boubnov, P. Röse, E. Saraçi, U. Krewer, J.-D. Grunwaldt, S. Cherevko, *ACS Catal.* **2021**, *11*, 9300.
[26] T. Audichon, E. Mayousse, S. Morisset, C. Morais, C. Comminges, T. W. Napporn, K. B. Kokoh, *Int. J. Hydrogen Energy* **2014**, *39*, 16785.
[27] H. Xu, Y. Han, Q. Wu, Y. Jia, Q. Li, X. Yan, X. Yao, *Mater. Chem. Front.* **2023**, *7*, 1248.
[28] R. Djara, M.-A. Lacour, A. Merzouki, J. Cambedouzou, D. Cornu, S. Tingry, Y. Holade, *Polymers* **2021**, *13*, 190.
[29] R. Djara, Y. Holade, A. Merzouki, N. Masquelez, D. Cot, B. Rebiere, E. Petit, P. Huguet, C. Canaff, S. Morisset, T. W. Napporn, D. Cornu, S. Tingry, *J. Electrochem. Soc.* **2020**, *167*, 066503.
[30] H. S. Kolla, S. P. Surwade, X. Zhang, A. G. MacDiarmid, S. K. Manohar, *J. Am. Chem. Soc.* **2005**, *127*, 16770.
[31] K. Kusada, H. Kobayashi, T. Yamamoto, S. Matsumura, N. Sumi, K. Sato, K. Nagaoka, Y. Kubota, H. Kitagawa, *J. Am. Chem. Soc.* **2013**, *135*, 5493.
[32] Y. Li, N. Li, K. Yanagisawa, X. Li, X. Yan, *Materials Research Bulletin* **2015**, *65*, 110.

[33] T. Audichon, B. Guenot, S. Baranton, M. Cretin, C. Lamy, C. Coutanceau, *Appl. Catal. B: Env.* **2017**, *200*, 493.
[34] T. Audichon, T. W. Napporn, C. Canaff, C. Morais, C. Comminges, K. B. Kokoh, *J. Phys. Chem. C* **2016**, *120*, 2562.
[35] R. Woods, *J. Electroanal. Chem. Interf. Electrochem.* **1974**, *49*, 217.
[36] C. C. L. McCrory, S. Jung, J. C. Peters, T. F. Jaramillo, *J. Am. Chem. Soc.* **2013**, *135*, 16977.
[37] S. Trasatti, O. A. Petrii, in *Pure Appl. Chem., Vol. 63*, **1991**, pp. 711.
[38] S. Trasatti, O. A. Petrii, *J. Electroanal. Chem.* **1992**, *327*, 353.
[39] M. E. Orazem, B. Tribollet, *Electrochemical Impedance Spectroscopy*, 2 ed., John Wiley & Sons, Inc. , Hoboken, New Jersey, USA, **2017**.
[40] A. Lasia, *Electrochemical Impedance Spectroscopy and its Applications*, Springer-Verlag, New York, NY, USA, **2014**.
[41] J. C. K. Ho, G. T. Filho, R. Simpraga, B. E. Conway, *J. Electroanal. Chem.* **1994**, *366*, 147.
[42] Y. Lai, Y. Li, L. Jiang, W. Xu, X. Lv, J. Li, Y. Liu, *J. Electroanal. Chem.* **2012**, *671*, 16.
[43] J. O. M. Bockris, E. C. Potter, *J. Electrochem. Soc.* **1952**, *99*, 169.
[44] A. Lasia, *Int. J. Hydrogen Energy* **2019**, *44*, 19484.
[45] G. Lodi, E. Sivieri, A. De Battisti, S. Trasatti, *J. Appl. Electrochem.* **1978**, *8*, 135.
[46] M. Chatenet, J. Benziger, M. Inaba, S. Kjelstrup, T. Zawodzinski, R. Raccichini, *J. Power Sources* **2020**, *451*, 227635.
[47] S. Anantharaj, S. Noda, M. Driess, P. W. Menezes, *ACS Energy Lett.* **2021**, *6*, 1607.
[48] D. Li, C. Lin, C. Batchelor-McAuley, L. Chen, R. G. Compton, *J. Electroanal. Chem.* **2018**, *826*, 117.
[49] L. A. De Faria, J. F. C. Boodts, S. Trasatti, *J. Appl. Electrochem.* **1996**, *26*, 1195.
[50] S. Fierro, A. Kapałka, C. Comninellis, *Electrochem. Commun.* **2010**, *12*, 172.
[51] J. Rossmeisl, Z. W. Qu, H. Zhu, G. J. Kroes, J. K. Nørskov, *J. Electroanal. Chem.* **2007**, *607*, 83.
[52] R. Djara, Y. Holade, A. Merzouki, M.-A. Lacour, N. Masquelez, V. Flaud, D. Cot, B. Rebiere, A. van der Lee, J. Cambedouzou, P. Huguet, S. Tingry, D. Cornu, *Front. Chem.* **2020**, *8*, Article 385.
[53] J. Rodríguez-Carvajal, *Phys. B: Condens. Matter* **1993**, *192*, 55.
[54] D. Zagorac, H. Muller, S. Ruehl, J. Zagorac, S. Rehme, *J. Appl. Cryst.* **2019**, *52*, 918.

Generally, the synthesis of metal particles requires reducing conditions to convert metal cations to zero-valence metals, which is incompatible with metal oxides, which require oxidizing conditions to reach a more oxidized state. Here, we report the polymerization-calcination methodology that enables the efficient synthesis of bimetallic metal-oxide materials based on Ir-Ru-$Ir_xRu_{1-x}O_2$, which catalyzes both hydrogen and oxygen evolution reactions.

Sarra Knani, Perla Hajjar, Marie-Agnès Lacour, Arie van der Lee, Erwan Oliviero, Eddy Petit, Valerie Flaud, Julien Cambedouzou, Sophie Tingry, Teko W. Napporn, David Cornu,* and Yaovi Holade*

A Route to Complex Materials Consisting of Multiple Crystalline Phases Ir-Ru-$Ir_xRu_{1-x}O_2$ as Multifunctional Electrocatalysts